Remote Sensing and Geovisualization of Rock Slopes and Landslides

Davide Donati [1,*], Doug Stead [2], Emre Onsel [3], Jesse Mysiorek [4] and Omar Chang [2]

[1] Department of Civil, Chemical, Environmental, and Material Engineering, Alma Mater Studiorum—University of Bologna, 40126 Bologna, Italy
[2] Department of Earth Sciences, Simon Fraser University, Burnaby, BC V5A 1S6, Canada; doug_stead@sfu.ca (D.S.); omarc@sfu.ca (O.C.)
[3] SRK Consulting, Vancouver, BC V6C 1S9, Canada; eonsel@srk.com
[4] Clifton Engineering Group Inc., Calgary, AB T2C 5C2, Canada; jesse_mysiorek@clifton.ca
[*] Correspondence: davide.donati17@unibo.it

Abstract: Over the past two decades, advances in remote sensing methods and technology have enabled larger and more sophisticated datasets to be collected. Due to these advances, the need to effectively and efficiently communicate and visualize data is becoming increasingly important. We demonstrate that the use of mixed- (MR) and virtual reality (VR) systems has provided very promising results, allowing the visualization of complex datasets with unprecedented levels of detail and user experience. However, as of today, such visualization techniques have been largely used for communication purposes, and limited applications have been developed to allow for data processing and collection, particularly within the engineering–geology field. In this paper, we demonstrate the potential use of MR and VR not only for the visualization of multi-sensor remote sensing data but also for the collection and analysis of geological data. In this paper, we present a conceptual workflow showing the approach used for the processing of remote sensing datasets and the subsequent visualization using MR and VR headsets. We demonstrate the use of computer applications built in-house to visualize datasets and numerical modelling results, and to perform rock core logging (XRCoreShack) and rock mass characterization (EasyMineXR). While important limitations still exist in terms of hardware capabilities, portability, and accessibility, the expected technological advances and cost reduction will ensure this technology forms a standard mapping and data analysis tool for future engineers and geoscientists.

Keywords: mixed reality; virtual reality; multi-sensor datasets; rock mass characterization; rock core logging

1. Introduction

The analysis of the stability of rock slopes requires a careful characterization of the rock mass be performed. Intact rock parameters, such as uniaxial compressive and tensile strength, and characteristics of discontinuities, including orientation, persistence, and roughness, contribute to defining the quality of rock masses as well their deformability and strength [1,2]. Typically, traditional field techniques can be employed to systematically collect rock mass and discontinuity data [3,4]. However, local conditions, such as the activity of slopes, dense vegetation, and unstable terrain, can pose significant challenges, limiting or even preventing in situ data collection due to safety or accessibility concerns.

The development, particularly over the past twenty years, of ground-based and airborne remote sensing (RS) techniques [5] has the potential to allow these challenges to be addressed. RS methods provide a means to collect geological and structural data across large areas in a relatively short time and are therefore routinely used in rock mass and terrain characterization at various scales [6–9] as well as for monitoring purposes [10–16].

Terrestrial and airborne laser scanning (TLS and ALS, respectively, [17]) and digital photogrammetric methods, such as Structure-from-Motion (SfM, [18]), allow for the construction of three-dimensional models of rock slopes and outcrops, and they are the most widely employed methods for rock mass characterization. In particular, compared to traditional digital photogrammetric techniques, SfM has the advantage of not requiring camera calibration parameters to be known a priori [5], providing greater flexibility in terms of survey planning and type of digital camera [19].

Three-dimensional models, particularly those derived from TLS and SfM, can be used to identify and map discontinuity planes and traces as well as to derive data, such as orientation, persistence, and spacing [5,20]. Conversely, ALS datasets are particularly suited for terrain analysis and are routinely employed to perform structural analyses through slope-scale and regional-scale lineament mapping (e.g., [21]).

Infrared methods have also recently been introduced for the analysis of rock slopes. Infrared thermography (IRT) involves the analysis of the infrared radiation of an object, which is a function of its temperature [22]. IRT proved effective in the identification and mapping of groundwater seepage [23], open cracks [24,25], near-surface intact rock bridges [9], and in the analysis of thermal behavior (e.g., cooling index) and thermal anomalies of rock slopes and rock masses [26–28]. While IRT investigates the global electromagnetic emission in the infrared band (1 mm–700 nm range), hyperspectral imagery (HSI) is capable of capturing the electromagnetic radiation of objects across several (typically, several hundred) discrete wavelengths [29]. Since the electromagnetic radiation in the short-wave infrared range (SWIR, 1.1–3 μm) is diagnostic of the chemical and mineral composition of the material, HSI has been largely employed for airborne application (e.g., [30]), particularly in the mining exploration field (e.g., [31]). More recently, ground-based applications have been developed, allowing for the analysis of lithological variations along steep slopes [32,33] and along rock cores [34].

RS methods provide spatial coverage for geological data that is significantly greater than that available through traditional field methods, which are limited by terrain, height, and site accessibility. They also can provide a wealth of geological information, ranging from structural and geomorphic to lithological and mineralogical data, requiring effective visualization methods to enhance the interpretation, communication, and sharing of these extensive datasets. In this sense, advanced mixed and virtual reality methods can be employed to optimize combined visualization and interpretation of advanced datasets. Conventional reality and complete virtual immersion are located at the far ends of the "reality-virtuality (RV) continuum" [35] (Figure 1).
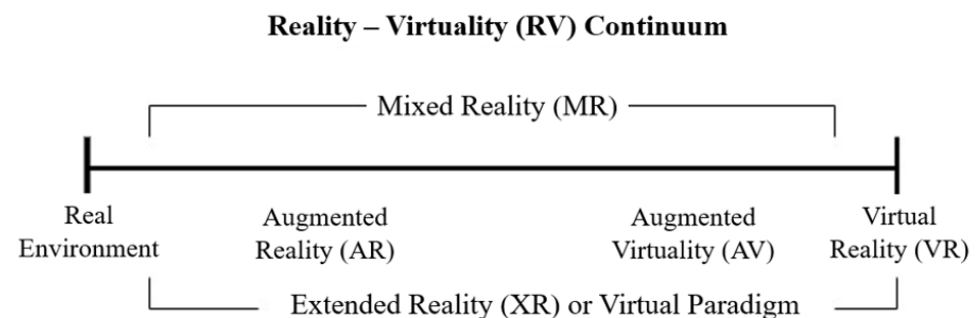
Figure 1. The Reality-Virtuality (RV) continuum (modified from [35]).

In particular, the virtual reality (VR) entails the complete overlay of a real environment by an interactive computer-generated environment that stimulates sensory responses (i.e., vision and sound), generally achieved using VR devices (e.g., VR goggles, headsets). Within the virtuality continuum, a progressive transition exists between the two "extreme" environments, entailing the presence of various combinations between reality and virtuality. Augmented Reality (AR) involves the overlay of datasets within the user's field-of-view. Conversely, Augmented Virtuality (AV) involves the emplacement of real

objects into virtual environments. Mixed Reality involves the entire RV continuum, except for the real environment and VR (i.e., the end members), and involves the coexistence of real and virtual elements within the user's field-of-view. AR, AV, and VR together form the Extended Reality (XR). Over the past decade, the application of MR and VR methods has increased significantly across various fields, including automotive [36], health sciences [37], production and manufacturing [38], and others. In the field of engineering geology, mixed and virtual reality have been introduced and applied, particularly for communication and remote collaboration purposes [39]. However, recent work has shown the potential application of these visualization methods for geotechnical data collection and processing [40,41].

In this paper, we demonstrate the challenges linked to the effective visualization of multiple RS datasets as well as the potential advantages in the application of MR and VR methods for the immersive visualization of integrated multi-sensor RS datasets of rock slopes. To do so, we describe the geological and geomechanical analyses conducted at various sites and various scales, highlighting, for each case, the importance of using a multi-sensor RS approach and the main challenges of the analysis, with an emphasis on those linked to dataset visualization. We present various methods and approaches for the processing and visualization of multi-sensor RS data and describe workflows for the collection and integration of RS datasets for three-dimensional visualization of rock slopes, both with traditional methods and within MR/VR systems. We describe MR/VR software applications developed for the advanced analysis and processing of RS datasets, including applications for performing virtual core logging, the three-dimensional visualization of rockfall simulations, and a mapping suite, created in collaboration with SRK Consulting® (Vancouver, BC, Canada), that allows seamless in situ rock mass characterization through discontinuity mapping and annotation.

2. Methods

2.1. Remote Sensing Equipment and Software

Data collection is performed using a variety of RS techniques and equipment, including laser scanning, digital photogrammetry, and infrared methods. Laser scanning data is collected using a Riegl VZ-4000 (Riegl, Horn, Austria) terrestrial laser scanner, TLS, with a maximum operating range of 4 km, and incorporating a 5 MPixel digital camera (to color the point cloud), a compass, a GPS, and an inertial measurement unit (IMU) to preliminarily register the point clouds in a three-dimensional space. Initial processing of the point clouds is performed using the proprietary software RiSCAN Pro 2.6 [42]. High-resolution photographs (HRP) are collected for texturing 3D models and to perform Structure-from-Motion photogrammetry using the software Metashape 1.5 [43]. Various DSLR cameras are employed in this study, including a 50 MPixel Canon EOS 5Ds-R, a 23 MPixel Canon EOS 5D Mark IV, and an 18 MPixel Canon EOS 7D equipped with an f = 200 mm prime lens or a f = 100–400 telephoto lens. At one of the sites, the Jure landslide in Nepal, a DJI Mavic Pro quadcopter, with a 12.7 MPixel camera, was used to collect aerial photographs. IRT datasets are collected using a FLIR SC7000 thermal camera, equipped with a f = 50 mm or, in some cases, a f = 100 mm focal lens. The SC7000 outputs raster images with a resolution of 0.41 MPixel (640 × 480), in which each pixel is associated with a temperature value, automatically computed by the instrument. Post-processing of thermal imagery and export in other file formats (e.g., jpg, tiff) are conducted using the software ResearchIR 4.4 [44]. HSI imagery is collected using a Specim SWIR3 hyperspectral scanner, which implements a 384-pixel push-broom sensor mounted on a rotating head. HSI datasets are processed using the software ENVI 5.5 [45] and following the processing workflow described in [32].

2.2. MR/VR Hardware

The MR system used for this paper includes both the first- and second-generation Microsoft HoloLens (HL) headsets. The first-generation HoloLens is a stand-alone MR system, characterized by an Intel Atom CPU, 2 GB RAM, 64 GB storage, running on a Windows Mixed Reality operating system. The HoloLens 2 is equipped with 4 GB RAM, Qualcomm Snapdragon 850 SoC. Overall, the second-generation HL provides an improved holographic density, a wider field of view compared to its predecessor (52° vs. 30°), eye tracking capability, and improved ergonomics and finger tracking. HL is characterized by lower computing power compared with VR systems, which can handle larger datasets, but must be tethered to an external workstation equipped with a compatible GPU. The VR system used in this paper is an HP Reverb Virtual Reality Headset, powered by an external, dedicated workstation, featuring an i7 CPU, two Nvidia 1080 GPU, and 128 GB RAM.

2.3. Workflow for Data Collection, Geovisualization, and Processing

Both traditional and innovative visualization methods for combined RS datasets are demonstrated in this paper. In all cases, three-dimensional datasets are used as a base on which multiple textures, constituted by rasters from multi-sensor RS datasets, are displayed (Figure 2). The workflow proposed in [46] is used to perform a bundle adjustment process, exploiting natural points observed on both the three-dimensional and two-dimensional raster datasets. The workflow takes advantage of the GPL (general public license) software GNU Octave 8.1 [47] and MeshLab 2022.02 [48], and allows high-resolution, multi-sensor textures to be created and registered onto meshes derived from three-dimensional datasets (e.g., TLS, SfM). Regardless of the sensor employed, a critical step was the export of the two-dimensional dataset to be exported using a standard format, such as JPEG or TIFF.

Three-dimensional models are then used to digitally characterize the rock mass and perform discontinuity mapping, using the software CloudCompare 2.12 [49]. Point clouds are used to perform the mapping and compute discontinuity orientation and persistence, whereas high resolution textures are used as supporting datasets (e.g., to resolve the trace of discontinuities and distinguish between discontinuity planes and brittle fracture surfaces). Where available, two- and three-dimensional, multi-temporal datasets are used to perform change detection analyses in order to investigate and monitor the morphologic evolution of slopes and other objects [7,50,51]. Three-dimensional meshes are simplified (e.g., the number of elements reduced) before undertaking numerical modelling analyses in order to avoid increased runtime due to excessive model geometry detail. Depending on the scale and size of the model, mesh simplification is performed prior to visualization and processing through MR or VR systems.

Computer applications for the visualization of RS data in MR and VR systems are developed using the game engine Unity and its built-in object-oriented programing language C# [52]. However, prior to bringing any model into Unity for MR and VR application implementation, the mesh of the model must undergo several preprocessing phases, including mesh simplification and reconstruction through software such as CloudCompare 2.12, MeshLab 2022.02, and/or Blender 2.93 LTS [53]. Optimizing the mesh is crucial to avoid significant reductions in frame rate (potentially causing the user to experience motion sickness), increased processing times, and system crashes. If the model remains (or is required to remain) too complex to be visualized using HL, it is reproduced through a VR application, which is only limited by the computational power of the workstation to which the system is tethered.
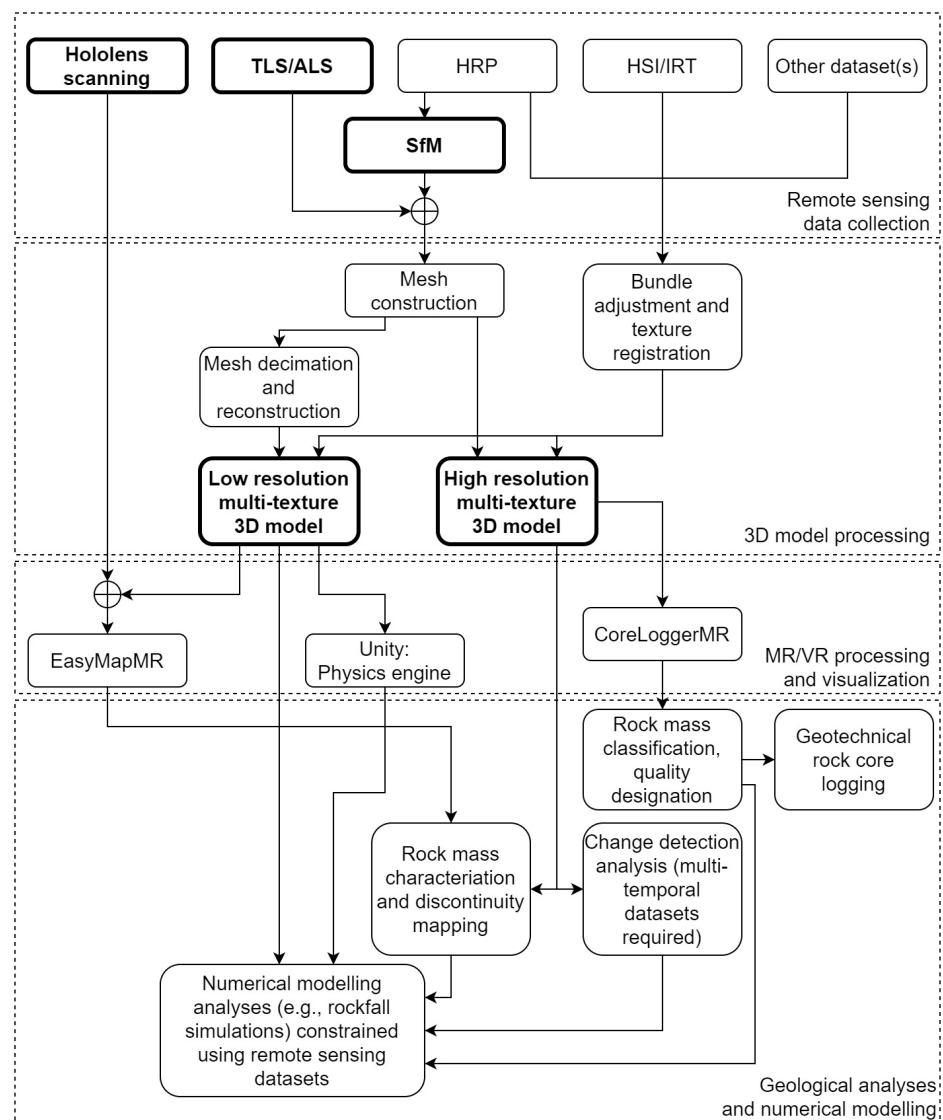
Figure 2. Workflow for the collection, processing, and geovisualization of RS datasets. Boxes with thick outline indicate three-dimensional datasets.

3. Results

In this section, the RS data collection and processing performed at various rock slopes and landslide sites is described. The analyses conducted at Yak Peak, British Colombia and Mt Kidd, Alberta in Canada, and Jure landslide, in Nepal, are described. At the Yak Peak, geological and structural analyses, including rock mass and brittle fracture characterization, were conducted through a traditional visualization approach. RS datasets collected at Mt Kidd, conversely, were processed and visualized using an MR approach. At the Jure landslide site, field and RS analyses were conducted. Multi-scale datasets were then visualized and processed using both traditional displays and an MR headset. Numerical modelling was also performed and visualized using an MR approach.
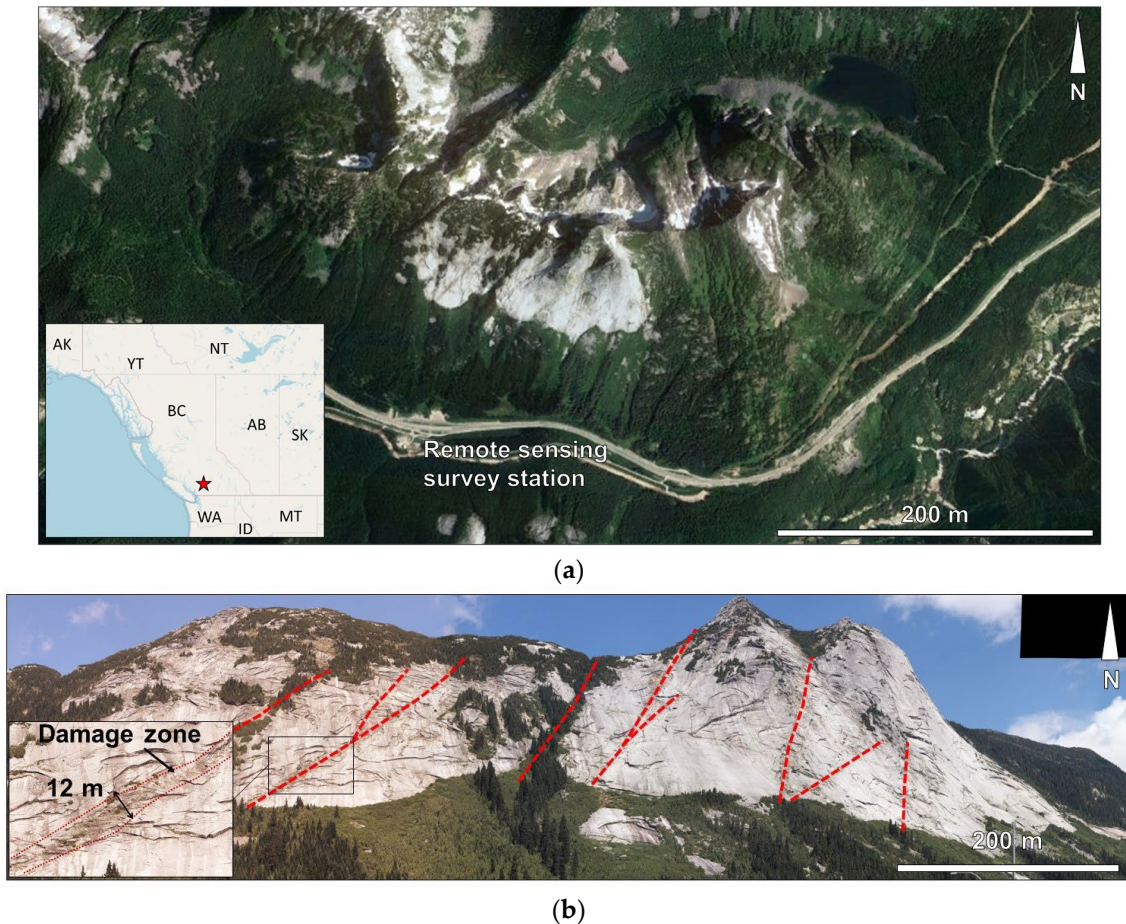
3.1. Yak Peak (British Columbia, Canada)

Yak Peak is a rock slope located in the Coquihalla Summit Recreation Area, along the Coquihalla highway, 30 km north of the municipality of Hope (BC, Canada). This 800 m high rock slope is formed by granodioritic intrusive rocks of the Needle Peak Pluton that crystallized during the Eocene era [54,55].

The investigated slope dips towards the south (195°) at an angle varying from 35° at the base of the slope to 55° in the upper part. The slope is intersected by several geological

structures (i.e., faults) that dip predominantly towards the northwest (Figure 3a). The rock mass forming the slope is massive, but rock mass quality decreases near the north-west dipping faults, indicating the presence of 10 to 30 m wide damage zones surrounding these geological structures (Figure 3a).

(**a**)

(**b**)

Figure 3. (**a**) 2022 satellite image of the Yak Peak (from Google Earth). The location from which the remote sensing datasets were collected is indicated. In the inset, the red star shows the location of the site in British Columbia (Canada). (**b**) Panoramic image of the slope. Dashed, red lines mark the NW dipping geological structures that intersect the slope. The inset shows a detail of the damage zone surrounding these geological structures.

Remote Sensing Analysis

The focus of the analysis conducted at the Yak Peak included (a) a preliminary discontinuity mapping, and (b) the analysis of brittle fracture features generated by the propagation of exfoliation joints at the surface of the slope.

RS datasets collected at this site include TLS, high resolution imagery, IRT, and HSI. All the sensors were located at the base of the slope on the opposite side of the highway, at a distance ranging from 900 m (at the base of the slope) to 1900 m (at the crest).

Discontinuity mapping was conducted using the TLS point cloud. Three discontinuity sets were identified: the exfoliation joints, E, parallel to the slope, with orientation 36°/192° (in the paper, discontinuity orientation is reported in dip/dip direction); J1 (49°/298°); and J2 (42°/041°). In particular, exfoliation joints were noted to act as a potential basal release surface for tabular blocks, whereas J1 and J2 act as rear release surfaces (Figure 4a).
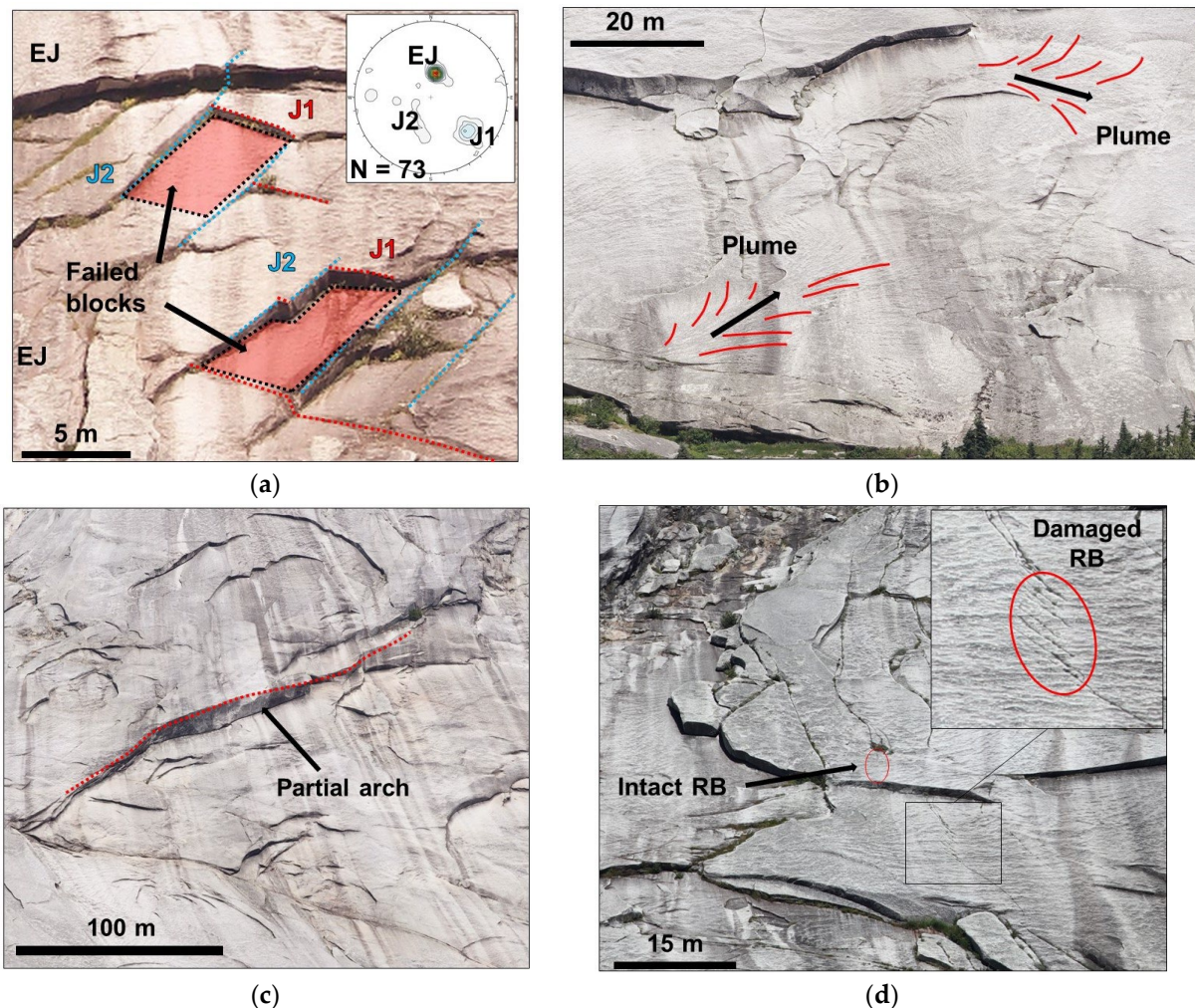
Figure 4. Overview of the structural and damage analyses at the Yak Peak: (**a**) Summary of the results of the discontinuity mapping performed on the TLS dataset (discontinuity sets marked by dashed lines with different colors). Note the tabular shape of the blocks generated by the intersection of the various discontinuity sets (highlighted in red). In the inset, the stereonet (equal area, lower hemisphere) is shown. (**b**) Plume features observed along the surface of exfoliation joints (marked by red lines). Black arrows indicate the expansion direction. (**c**) Example of a "partial arch" observed along the rock slope (marked by the dashed red line). (**d**) Rock bridges (RB) at various stages of failure. In the inset, a damaged RB: note the en-echelon fracture that formed along its length.

The high-resolution photographs allowed brittle fracture features to be highlighted across the slope. In particular, "plume/feather" features were noted along the surface of exfoliation joints (Figure 4b), whereas "partial arches" formed the steps that are visible across the slope (Figure 4c). Plumes and partial arches are both features that typically form as a result of sudden, brittle propagation of fractures in rock [56]. However, it is challenging to infer the time of formation of such features and to thus evaluate whether they are the result of the progressive cool down of the pluton after its emplacement or, alternatively, the stress relief following the exhumation of the plutonic rocks (e.g., [57]).

Various rock bridges at varying stages of damage were also identified: intact (no fracturing evidence observed along the rock bridge), damaged (single or cluster of cracks observed within the intact rock of the rock bridge), and failed (presence of a fully persistent fracture across the originally intact rock) (Figure 4d).

IRT dataset was collected with the FLIR SC7000 coupled with the f = 50 mm focal lens. Thermal data showed limited or no seepage across the slope, likely due to the absence of significant rainfall events in the days preceding the survey (28 August 2017). A significantly

wetter area was noted, however, at an outcropping area in the lower part of the slope (inset in Figure 5a). At least part of the seepage appeared to come from an exfoliation joint, which may be fed by the fracture network located below the water table.

(a)

(b)

(c)
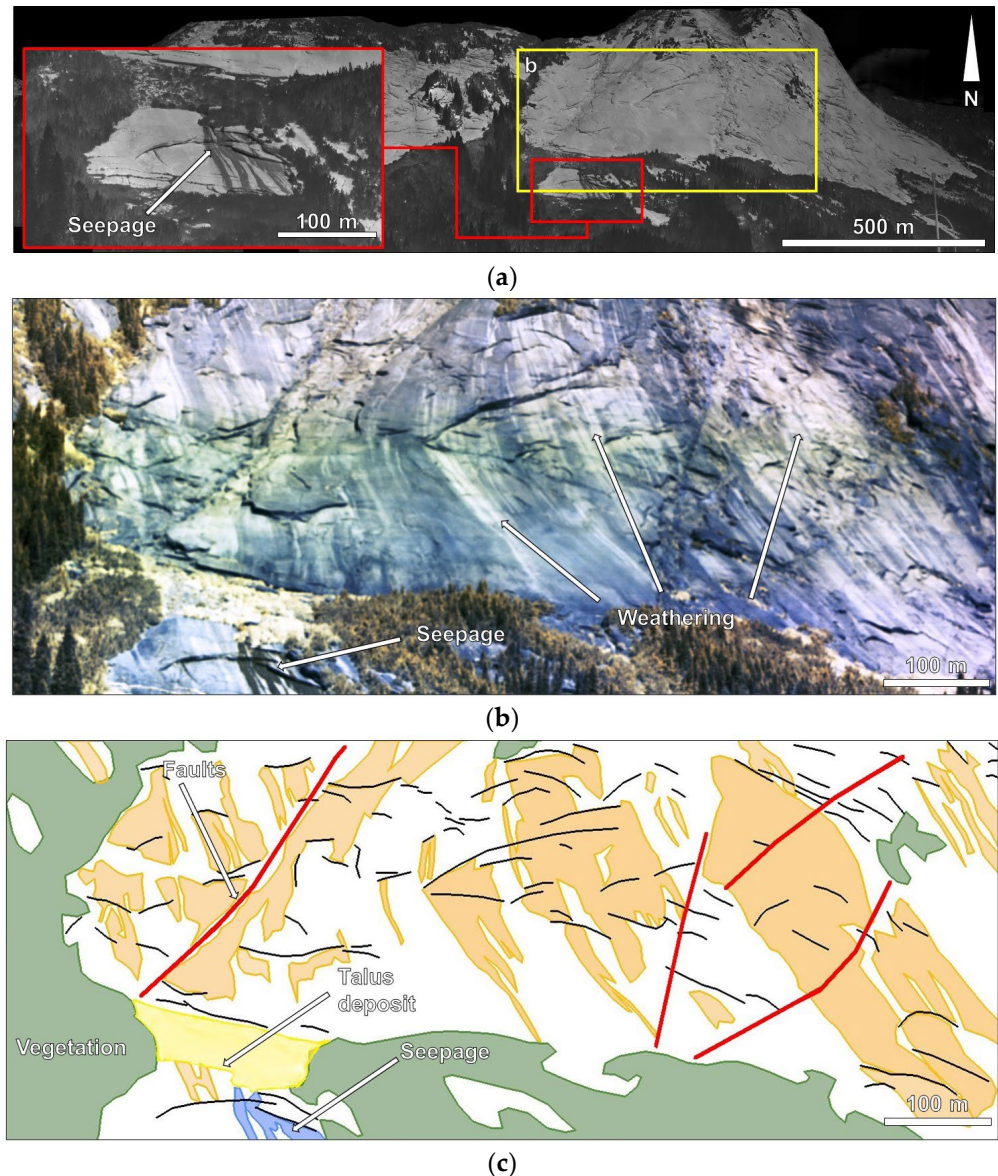
Figure 5. Detail of the infrared datasets collected at the Yak Peak: (**a**) IRT dataset, displayed in greyscale. Darker tones indicate colder temperatures. The inset magnifies the area in the lower part of the slope where seepage is observed. Yellow box outlines the area depicted in (**b**,**c**). (**b**) Detail of the HSI dataset, showing variability in electromagnetic irradiance along the slope surface (unclear origin, e.g., seepage and runoff water during and after rainfall events, lichen growth, and newly exposed surface), and the seepage in the lower part of the slope. (**c**) Sketch map highlighting the various materials and features that can be distinguished in the high-resolution photograph. The map highlights the role of partial arches and other structural features (marked by the black curves) in controlling the spatial distribution of weathered or altered surfaces (orange areas).

The HSI dataset allowed different degrees of weathering across the slope to be identified. Changes in the degree of weathering were observed throughout the slope, which resemble areas of seepage and surficial water flow during prolonged rainfall (Figure 5b,c). Specifically, the radiance of the slope appears to increase where surficial flow typically occurs compared to areas that remain predominantly dry. The absence of spectral targets at

the slope surface prevented the calibration of the HSI image, and a mineralogical classification of the surface was thus not performed. As a result, it is currently unclear whether this is due to variable mineral alteration or lichen growth, and further field and/or laboratory analyses should be undertaken to verify and validate the long-range hyperspectral survey results. Spatial correlations with newly exposed areas where recent rock block detachment occurred, potentially associated with fresh, unaltered surfaces [58,59], may also be investigated using multi-temporal datasets.

### 3.2. Mt. Kidd (Alberta, Canada)

Mt. Kidd is an iconic mountain peak located in south-eastern Alberta (western Canada), within the Kananaskis National Park, 70 km west of the city of Calgary (Figure 6a). The most prominent feature of Mt. Kidd is the namesake syncline fold that forms its southernmost peak, which can be observed from the flood plain of the Marmot Creek along Highway 40 (Figure 6b,c).
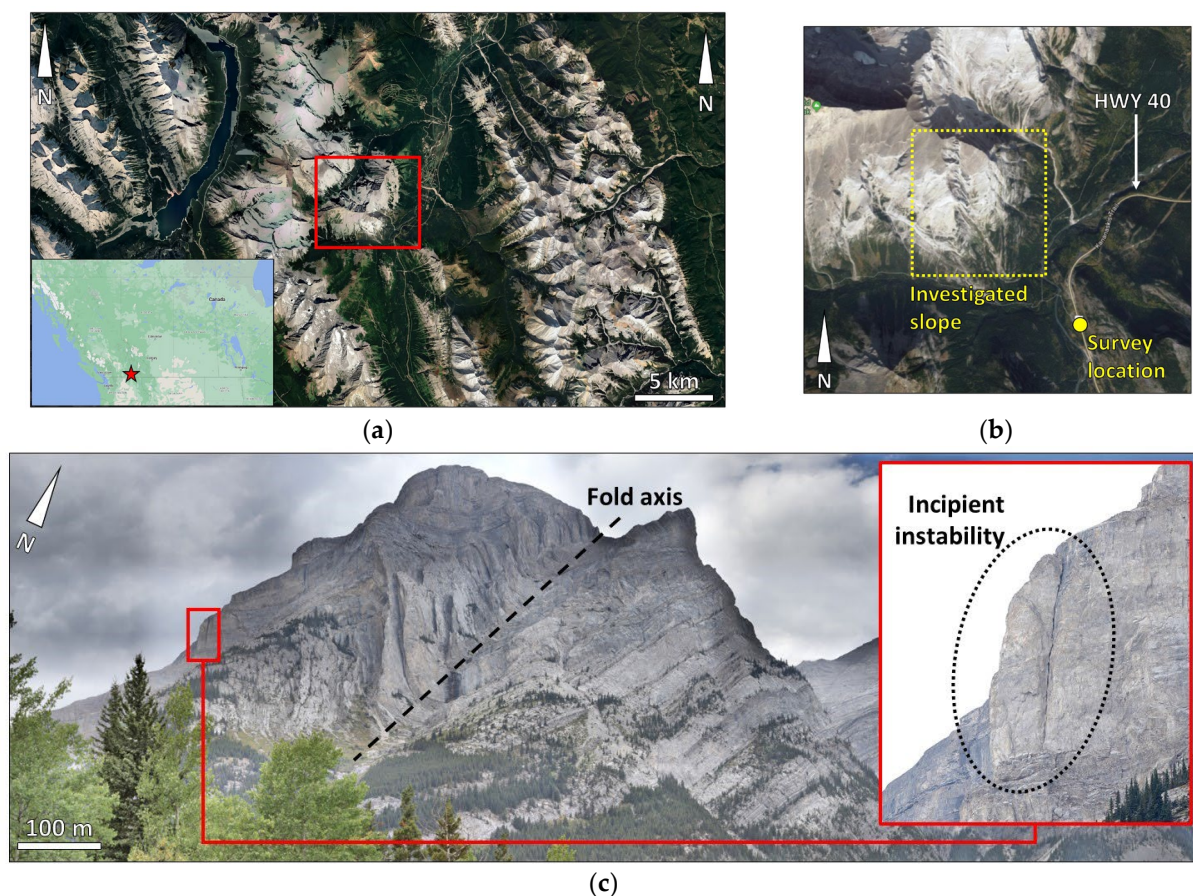
Figure 6. Overview of Mt. Kidd area: (**a**,**b**) location of Mt. Kidd in western Alberta (Canada) near the border with British Columbia (red star in the inset), with the red square outlines the area depicted in (**b**); (**b**) location of the survey location (yellow dot) with respect to the investigated slope (outlined in yellow); and (**c**) view of the Mt. Kidd syncline from South. The inset shows an example of incipient instability promoted by the structural setting.

The syncline involves the limestone, shales, siltstones, and dolostone of the Etherington, Mount Head, Livingstone, and Banff formations, which are Mississippian in age (359–323 million years) [60]. The syncline occurs at the termination zone of the Lewis Thrust, which formed in relation to the east-west tectonic compression, caused by terrane accretion, that resulted in the formation of the Canadian Cordillera [61,62]. The rock slope where the syncline is displayed extends between the elevations of 1500 and 2700 m a.s.l., with a slope angle varying between 30° and 35°.

At the Mt. Kidd site, we collected TLS, HRP, IRT, and HSI data (see Section 2.1 for details on the equipment used). A three-dimensional mesh was created from the TLS point cloud. The other two-dimensional datasets were used to create textures, which were then parametrized (i.e., registered) onto the mesh using the software Meshlab 2022.02. The multi-texture model was then exported in a wavefront ".obj" format and visualized in the HL headset using a viewer application specifically developed in Unity. The data collection at Mt. Kidd was performed in order to demonstrate the ability to visualize a multi-sensor dataset using the HL dataset (Figure 7).

(**a**)

(**b**)

(**c**)
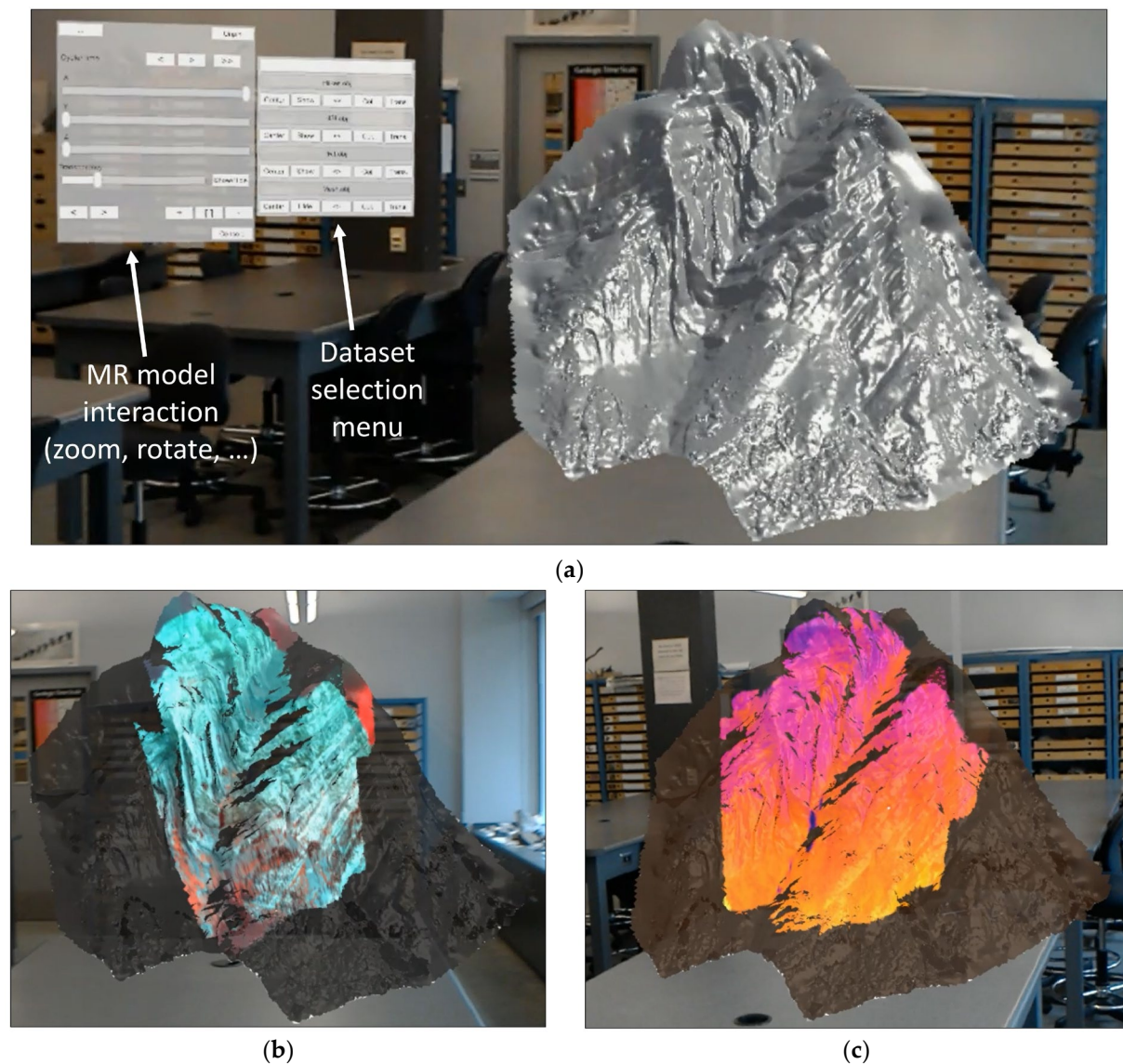
Figure 7. MR visualization of the RS datasets collected at Mt. Kidd: (**a**) three-dimensional mesh of Mt. Kidd, derived from the TLS. The MR interface, which allows for texture toggling and model zooming and rotation, is visible (photographs were obtained using the HL in-built digital camera); (**b**) model with HSI texture; and (**c**) model with IRT texture. In (**b**,**c**), the holes within the texture are due to the occlusions due to the RS survey location.

Potential applications of the three-dimensional model may include (a) a detailed, multi-scale, from slope- to outcrop-scale, discontinuity mapping; (b) a characterization of fracture intensity distribution, aimed at the investigation of its spatial variation as a function of the distance from the fold axis; and (c) the analysis of changes in layer thickness to demonstrate the application of RS methods in the classification of structural geological

folds. Additionally, the combination with high-resolution photography can potentially allow for the investigation of incipient rockfall and other slope failures, based on visual examination of the datasets (inset in Figure 6c).

3.3. Jure landslide (Nepal)

The Jure landslide is a large 5.5 million m^3 destructive landslide which occurred on 2 August 2014, near Jure village, on the right slope of the Sunkoshi River valley in central Nepal, 70 km northeast of Kathmandu (Figure 8a). The landslide involved low-grade metamorphic rocks (phyllite, phyllitic quartzite, and metasandstones) of the Kuncha formation, which is part of the Lesser Himalayan tectonic zone [63–65]. Several houses were destroyed, and the slope failure resulted in about 150 fatalities. The landslide deposit dammed the Sunkoshi River, and a 3 km long landslide lake formed, which damaged hydropower plants both upstream and downstream before the dam was artificially breached after 37 days [66]. An historical analysis conducted using satellite imagery highlighted that an active slope deformation, which resulted in multiple, smaller mass wasting events, was ongoing prior to the detachment of the 2014 landslide [67].

(a)

(c)

(b)
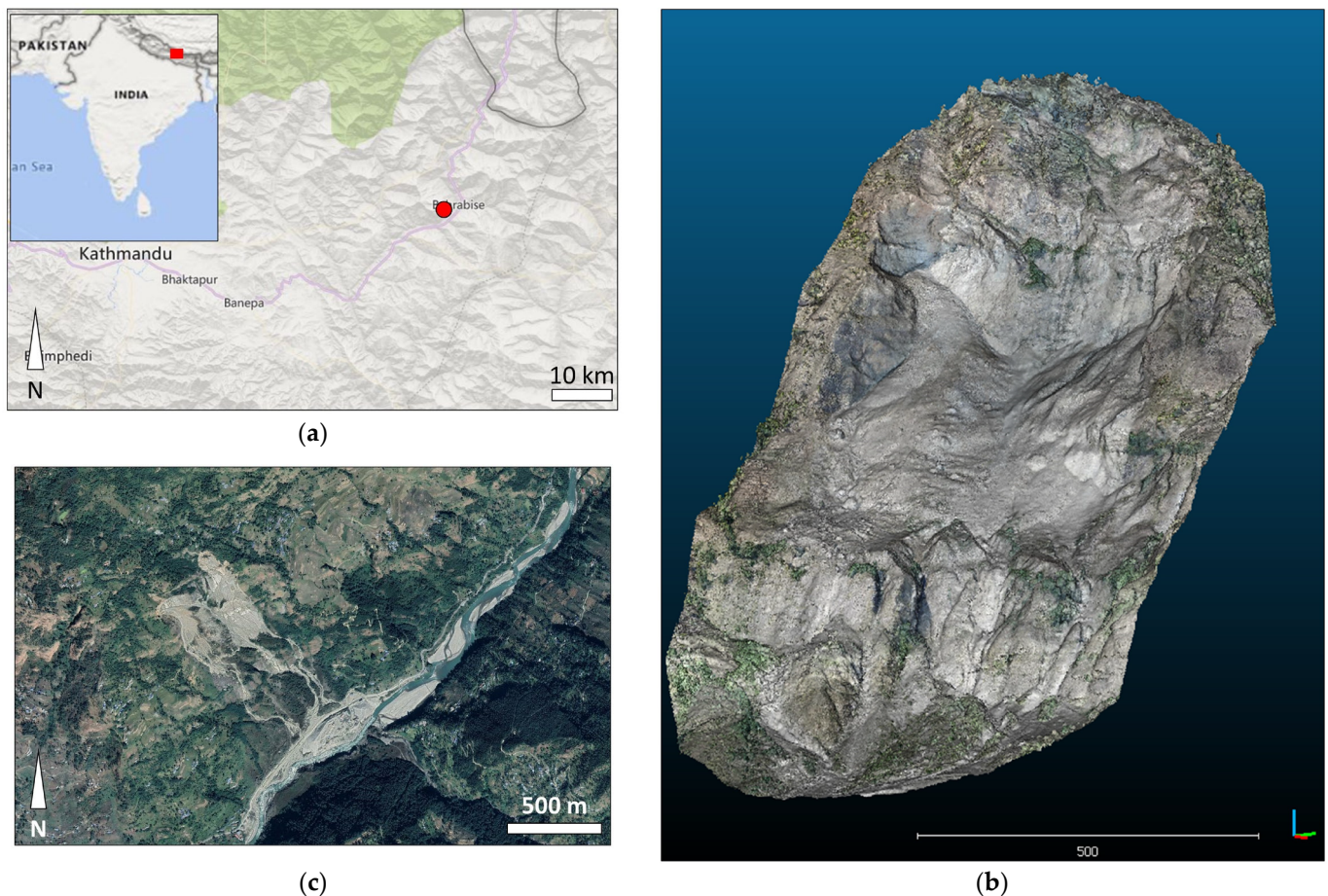
Figure 8. Overview of Jure landslide: (**a**) location of the study area within Nepal's province of Bagmati in the Indian subcontinent (inset); (**b**) 2020 satellite image of the landslide area (CNES/Airbus image); and (**c**) 2018 UAV-SfM three-dimensional of the landslide. Note the growth of scree and vegetation in the lower slope in (**b**) compared to the earlier three-dimensional model.

The landslide has a surface area that extends 1500 m downslope and 500 m across, between an elevation of 1575 m a.s.l. and the valley floor at 800 m a.s.l. The average slope angle prior to the failure was 35° (Figure 8b).

The structural setting of the area is characterized by pervasive faulting in an E-W orientation. The most important geological structures are represented by three regional faults: the Main Frontal Thrust (MFT), the Main Boundary Thrust (MBT), and the Main Central Thrust (MCT). The activity of these faults causes the rock mass to appear intensely foliated, folded, and fractured [64].

3.3.1. Remote Sensing Analysis

At the Jure landslide site, various RS datasets were collected at different times. Yearly long-range, ground-based photogrammetric and TLS surveys were conducted between 2016 and 2019. Both TLS and ground-based HRP were collected from multiple stations along the valley floor and from the opposite slope. Airborne HRP was also collected in 2016 from a helicopter, and in 2018 and 2019 using the DJI Mavik Pro UAV (Figure 8c). HRP datasets were used to create panoramic images and three-dimensional SfM models in Metashape.

Long-range terrestrial and airborne SfM and TLS datasets were used to perform slope scale discontinuity mapping in CloudCompare 2.12. TLS datasets provided, in general, a higher point density, although distinguishing smaller features remained a significant challenge, which could be ameliorated by overlaying the SfM-derived textured mesh.

Slope-scale discontinuity mapping allowed major structural features to be mapped. It was noted that the landslide scar is crossed by various structural features that potentially controlled the extent and failure mechanism of the landslide. The southern and northern release surfaces appear to be controlled by two sets of structural features, referred to as SL1 and NL1, with orientation of 43°/052° and 65°/240°, respectively. A major structural feature, X1, also crosses the landslide scar with an orientation of 46°/089°.

Rock mass jointing and foliation were also observed in the long range HRP datasets. These were investigated using the SfM-derived three-dimensional model of an outcrop in proximity to the landslide headscarp, built through a short range HRP survey. An outcrop scale discontinuity mapping, performed in CloudCompare 2.12 using the "Compass 2.0" plugin [68], allowed four discontinuity sets (DS-I to DS-IV) to be identified. DS-I, DS-II, and DS-IV are high angle discontinuity sets with orientation 80°/180°, 80°/110°, and 60°/250°, while DS-III represents the sub-horizontal foliation.

The multi-temporal RS surveys allowed for the post-landslide evolution of the slope to be investigated. It was noted that significant instability characterized the headscarp in the years after the main landslide. A change detection analysis conducted using the 2017, 2018, and 2019 datasets, considering the 2016 dataset as reference, evidenced a progressive retrogression of the headscarp. In total, about 440,000 m^3 of material detached from the upper slope between 2016 and 2019, with a peak between 2016 and 2017, when mass wasting events involved a total volume of 230,000 m^3. Figure 9a shows the changes that globally affected the slope from 2016 to 2019.

3.3.2. 2D Rockfall Simulations

The code Rocfall2 [69] was used to perform rockfall simulation in two dimensions. The simulations were conducted using a representative section, extracted from the RS datasets using the profile tool in ArcMap [70] along the average maximum steepness of the slope. The considered section was traced starting from the primary rockfall source area identified through the RS change detection analysis. Coefficients of restitution were assigned to the various parts of the section, depending on the type of hillslope material (bedrock, talus, and talus with vegetation) identified based on field observation and a visual analysis of the RS datasets [67]. The size and shape of the blocks considered for the simulations derived from a point cloud analysis. Block angular and translational velocities as well as bounce height can be tracked along the rockfall trajectory from detachment to full stop [67].

Rockfall simulation results, for the considered section, showed a maximum bounce height (i.e., distance between block and ground surface, measured along the vertical direction) of 65 m at the source area, and another peak (45 m) immediately below a morphological step in the lower slope. Translational velocity profile displayed significant undulations in value and peaks at 75 m/s, while angular velocity increased constantly after block detachment and peaked at 140 rad/s. Peaks for both translational and angular velocities occurred at the impact of the block following the 45 m peak in bounce height.

(**a**)   (**b**)
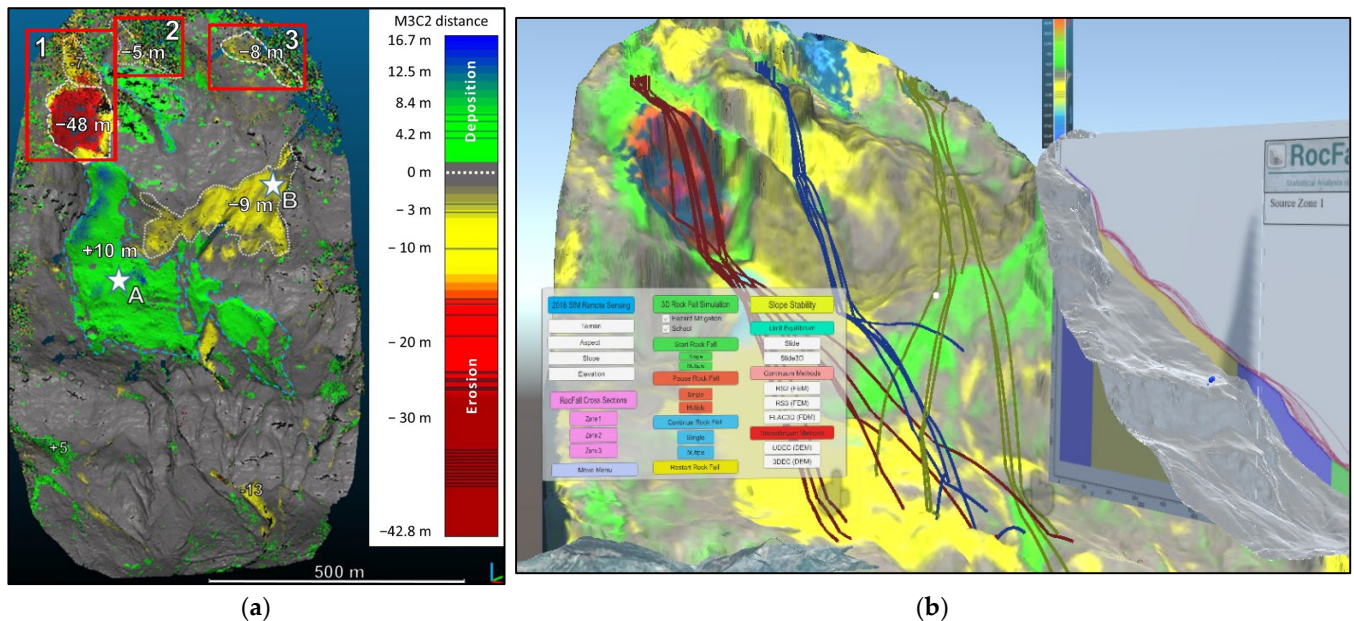
Figure 9. Application of the three-dimensional datasets for change detection and rockfall modelling. (**a**) Results of the slope scale change detection analysis, conducted using the M3C2 approach. The red squares (1–3) show the areas of the landslide crown where most of the geomorphic evolution occurred. The enclosed values indicate the 2016–2019 computed surface change. The stars (A,B) indicate areas within the landslide area where generalized erosion or deposition occurred within the same time window. (**b**) Overview of the rockfall numerical simulation developed in Unity game engine. Rockfall sources are selected based on the results from the change detection analysis. The holographic interface also includes a menu to control visualization parameters and object visibility (to the left) as well as the results from two-dimensional rockfall simulations conducted in RocFall2 (to the right).

3.3.3. MR Rockfall Simulations

The models collected using RS methods were used as input geometry for three-dimensional rock fall simulations conducted using the Unity game engine, exploiting the state-of-the-art, built-in physics engine that is capable of realistically simulating the collision between solid bodies, which, in this case, are the falling block and the ground surface. In the models, terrain colliders and material physics were used to indirectly set varying coefficients of restitution across the slope surface as a function of surface materials.

Rockfall source areas were assigned in the model based on the results of the change detection analysis, which identified three areas where material detached over the 2016–2019 time window. Rockfall simulations were displayed in MR using the Microsoft HL headset (Figure 9), allowing for up- and down-scaling of the model, the observation of the rockfalls as the blocks move down the slope, overlay of multiple RS datasets and analyses (e.g., change detection results), and additional numerical models [51].

Results of two-dimensional rockfall simulations were also imported in raster format into Unity in order to perform a direct comparison between the two modelling approaches (Figure 9). A good agreement was noted between the two- and three-dimensional simulation results. Only marginal differences were noted in translational velocity and bounce height, which were slightly higher in the three-dimensional models compared with two-dimensional simulations in Rocfall, and in rotational velocities, which were slightly higher in the two-dimensional analysis.

4. Potential Future Applications of MR and VR for Rock Mass Characterization and Real-Time Data Collection and Processing

The capability of support and assistance (even in real time) from experienced professionals, and the capability of the chosen technique to allow datasets to be reviewed and the site to be digitally (or virtually) revisited, can have significant, positive impacts on the reliability of geological data and interpretations. In this section, two innovative software applications for data collection exploiting MR and VR are presented, which can potentially assist in data collection, processing, and interpretation: the mapping suites "CoreLogger MR and XRCoreShack" and EasyMineXR. The presented software, particularly EasyMineXR, is currently undergoing field testing at various mine sites. The results of such testing and the description of cases studies involving real time MR mapping will be presented at a later stage.

4.1. CoreLogger MR and XRCoreShack

CoreLogger MR is a novel software application that was developed for use with Microsoft HL and core logging. The app allows the user to log physical cores, through an MR interface that includes a holographic logging sheet in which values and parameters are inputted through a virtual or a Bluetooth keyboard (Figure 10a). Graphical numerical data sheets, such as RMR and GSI, can also be clicked holographically to store representative values for specific intervals. The HoloLens 2 finger tracking capabilities are also used to acquire RQD values holographically by using them as pivot points (Figure 10b). The user can also take advantage of the MR mesh scanning proficiency to acquire RQD values directly along the core by placing the anchor point directly on the core samples holographically.
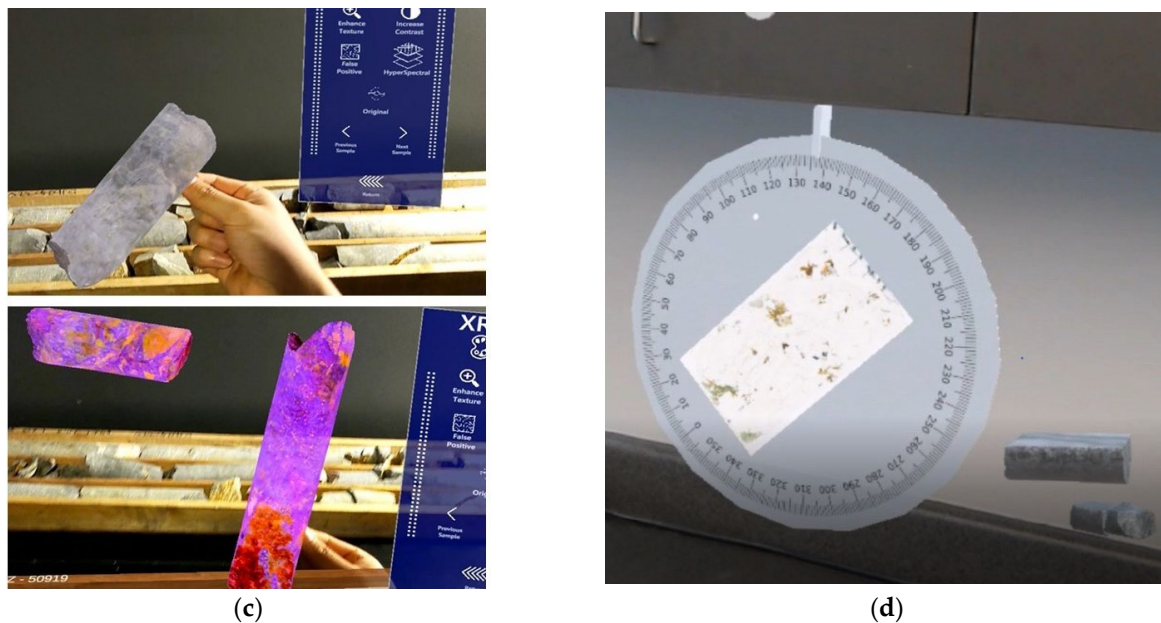

(**a**)

(**b**)

Figure 10. *Cont.*

(**c**)   (**d**)

Figure 10. Overview of geotechnical holographic core logging: (**a**) geotechnical core logging performed with the CoreLoggerXR app, showing the interactive menus for data entry; (**b**) measurement of the length of a rock core piece for RQD estimation; (**c**) section of a holographic core piece imaged using optical (above) and hyperspectral sensors (below), with the hyperspectral model shown in false colours; and (**d**) example of virtual thin section visualized within the MR app.

Individual cores and the whole core box can be digitized in 3D, using novel software known as XRCoreShack. Within this software, multi-sensor core datasets can be superimposed along and on the virtual core (Figure 10c). Datasets tested to date include thermal, hyperspectral, FMI (full-bore formation microimager), assays, and previously constructed core logs. The mesh can also be manipulated to observe structures and mineralization that are not easily visible with the naked eye. The virtual thin section, previously scanned and imaged, can also be implemented within the core database for improved visualization (Figure 10d).

CoreLogger MR combined with XRCoreShack enables holographic core logging. XR-CoreShack has been implemented within VR platforms, allowing multiple core samples to be assessed simultaneously, and enabling the comparison of different core boxes side-by-side.

With recent advances in MR/VR and the development of XRCoreShack, re-examination of core runs can be performed remotely, holographically, or virtually. Reliance on digitizing core data has proven to be useful for auditable supervision, depth adjustment via downhole geophysics, and rock parameter segregation via multi-disciplinary assessment [71]. Furthermore, allowing core loggers to limit multi-step logging procedures can reduce the uncertainty and errors associated with digitizing information from paper records.
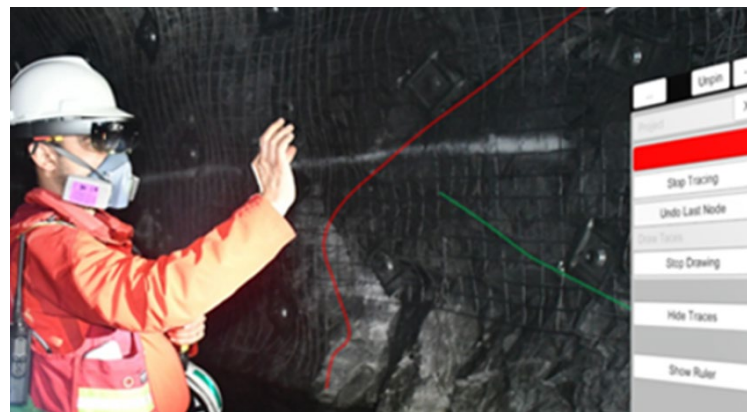
4.2. EasyMineXR

EasyMineXR (EMXR) is a Microsoft HL application developed under a joint Mitacs Accelerate project between SRK Consulting Vancouver and Simon Fraser University, and later commercialized [72,73].

EMXR uses the built-in 3D scanner of the Microsoft HL to capture data on site. The Microsoft HL scanner creates a mesh of the object with a resolution of about 5 cm when observed by the user from a distance of 0.8 m to 3 m. The engineer or geoscientist can create a mesh in near-real time by walking along and looking at the outcrops of interest. The user can also view, hide, and colorize the mesh. After completing the scan, the user can see a small-scale preview of the mesh and save the 3D dataset. Georeferencing can be conducted using a compass and a survey point or two survey points. Once the registration process is

completed, the local HL coordinate system will be converted to a real-world coordinate system. The georeferenced data, such as meshes and drillhole data from Leapfrog Geo [74] after importing into EMXR, will appear in their real-world coordinates, allowing the user to visualize previously collected data and make more advanced interpretations on site.

The software allows users to map geological, structural, and geomechanical features by drawing polylines along them (Figure 11a). The user can specify the type of feature before saving the trace and can also add annotations to the shape using a data-entry form that appears when the 3D polyline is selected. The data-entry form template varies depending on the structure type (e.g., lithological contact, fault, or joint). Traces are exported directly as georeferenced .csv or .dxf files to geological and mining software without any post-processing.

(**a**)
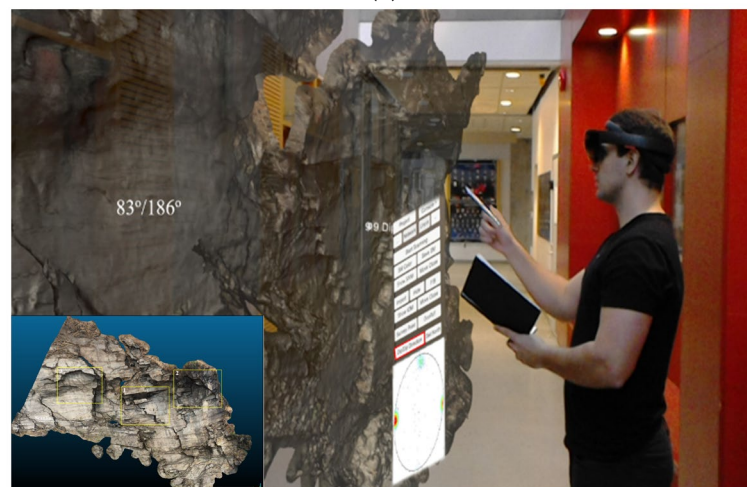
(**b**)

Figure 11. Application of EasyMineXR for rock mass characterization: (**a**) real-time geological mapping conducted in an underground setting; (**b**) off-site office-based rock mass characterization in EMXR, using a three-dimensional model built using RS data collected at the Jure landslide site. In the inset, a view of the slope model that is being investigated.

For discontinuity mapping, an orientation tool has been developed that can measure the dip and dip direction of the discontinuity facets. Orientation of the discontinuity surfaces is displayed when the users look directly at them. This data can be saved and displayed on a stereonet by an air tap hand gesture. A Fuzzy K-mean algorithm [75] can also be used to determine the discontinuity sets. Collected orientation data can be exported as .csv file for use in geotechnical and geological software. Current on-site mapping methods require geologists and engineers to physically place their compasses or cell phones on

the rock face, which can be a slow process, and often comes with associated safety issues. EMXR improves speed and safety by not requiring users to touch the outcrop.

Finally, EMXR can take photographs and record videos. It can also show charts, such as Barton and Choubey's joint roughness profiles [76]. For measuring structure sizes, a ruler tool is also available to the user.

EMXR can collect and process geomechanical and structural data in the field directly, but it can also import three-dimensional models from other RS methods (e.g., TLS, SfM). This enables users to remotely (re)visit sites and perform or review rock mass characterization and discontinuity mapping. In Figure 11b, the model of an outcrop behind the headscarp of the Jure landslide is visualized with the EMXR app in a safe environment. A comparison of field, RS computer-based software and holographic discontinuity mapping along the same rock slope shows a mean pole orientation difference of about 5° between discontinuity sets [51].

5. Discussion and Conclusions

Over the past two decades, advances in technology have allowed the visualization, processing, and interpretation of complex three-dimensional datasets. In particular, the capability of extracting geological information from models created using RS methods, such as TLS and digital photogrammetric techniques, represented a turning point both in professional practice and in academic research. Similarly, the recent development of MR and VR represents a potential breakthrough that allows datasets to be observed through an unprecedented immersive experience. Presently, however, the applications of these visualization techniques have been largely limited to communication and recreation (e.g., videogame industry), while applications of MR and VR for the purpose of data analysis and processing is still in an early stage of development. In this paper, we demonstrated that advanced, immersive visualization methods can be effectively used for data processing and real time rock engineering/geology data collection and interpretation (Table 1).

Table 1. Summary of the applications of various geovisualization methods described in this paper.

	Yak Peak	Mt. Kidd	Jure Landslide	XRCoreShack	EasyMineXR
Remote sensing data collection	• TLS • HRP • HIS • IRT	• TLS • HRP • IRT • HSI	• TLS • HRP • UAV-SfM	• HRP • SfM • IRT • HSI	• In-built HL scanning capability, remote sensing data import
2D/3D visualization and processing (on screen)	• Discontinuity mapping • Brittle damage • Seepage mapping	• Structural characterization * • Discontinuity mapping *	• Discontinuity mapping • Rockfall simulations	• Lithological and mineralogical characterization * • Discontinuity analysis *	Possibility to export HL scans to traditional visualization systems
MR/VR visualization	-	HSI, IRT datasets visualized as texture on 3D mesh from TLS dataset	• 3D holographic rockfall analysis • Landslide MR/VR database	2D remote sensing datasets visualized as texture on 3D mesh from SfM models	Visualization of remote sensing datasets from various sources (e.g., SfM, TLS)
MR/VR data processing	-	-	Outcrop scale MR/VR discontinuity mapping	Datasets visualized using MR/VR headsets, where mapping is undertaken	Immersive, MR rock mass characterization using remote sensing datasets and models
MR/VR real time data collection and processing	-	-	-	Real time rock core logging using virtual, interactive sheets and charts	Real time discontinuity mapping, annotation, stereonet analysis

*: potential applications not demomnstrated in this paper.

The digital visualization and processing of geological data are today almost exclusively conducted using traditional approaches (i.e., on screen). However, using MR and VR, particularly to visualize three-dimensional models derived from RS datasets, allows the

user to visit, walk around, and inspect outcrops that cannot be physically reached, and to perform rock mass characterization and discontinuity mapping in a safe environment. The ability to share the MR and VR experience in real time between people physically located at different locations can enhance both real-time collaboration between engineers and geoscientists as well as data visualization, providing significant improvements to the quality of geological investigation and interpretation. Indeed, despite the importance of rock mass characterization in the design of engineering structures, it is often conducted, in the field and by junior staff with limited experience. Even standardized procedures for rock mass and discontinuity classification and characterization, such as RQD (rock quality designation, [77]), Q-System [78], and GSI [2], have potential for human error and bias that can lead to crucial features being improperly logged (e.g., [79]). These errors may result in increased project costs and improper design. We suggest that shared, in situ MR experience can allow senior professionals to assist and train junior colleagues without being physically present in the field, significantly optimizing mentoring using the collected experience of consultants and reducing, at the same time, the potential for errors and bias.

Presently, the main challenge with the use of MR and VR methods lies in hardware capability and portability. VR headsets are not stand-alone systems but require tethering to a workstation: the specifications of the workstation control the quality and detail of the models that can be visualized (Table 2). Additionally, VR headsets allow for a full immersion in the virtual world, isolating the user from the real environment, potentially inducing motion sickness and even posing safety issues due to a diminished awareness of the user's surroundings. Conversely, MR headsets, such as Microsoft HoloLens, allow full portability and thus the use of the technology in the field. However, the miniaturization of the components leads to a limited computational capability, thus limiting the quality and dimension of the three-dimensional models that can be visualized at any given time.

Table 2. Summary of the main advantages and limitations of current VR and MR visualization methods.

	Advantages	Challenges
Virtual reality (VR)	• Fully immersive • High computational capabilities • Relatively low price range • High responsiveness controllers	• Possible motion sickness • Eye straining • Tethered to workstation • Fish-eye effect • Limited awareness of surroundings
Mixed reality (MR)	• Spatial awareness • Untethered, stand-alone system • Scanning capabilities (Microsoft HoloLens)	• Computational limitations • Battery life can be a concern • Relatively high price range

Significant advancements in MR technology may be linked to the miniaturization of an increasing number of powerful computer components, allowing for progressively more detailed and complex three-dimensional models to be visualized.

A significant current limitation is related to the limited availability of MR/VR commercial/open-source mapping software. In this paper, we presented EMXR, a Windows software that allows geomechanical mapping of outcrops. However, the use of MR technology for applications beyond rock mass characterization and discontinuity mapping may require custom programs to be designed and coded in C# within Unity (or other software or another game engine (e.g., Unreal Engine)) directly by the potential user, who needs to be (or become) familiar with computer programming and coding. However, it is expected that the increasing distribution of MR and VR headsets will accelerate the development and expand the availability of both proprietary commercial and open-source software for geotechnical applications.

The continuous development of RS techniques has greatly enhanced the ability of geoscientists and engineers to perform geotechnical and geomechanical analyses (e.g., rock mass characterization). Over the past two decades, however, it is apparent that these developments in data collection and processing procedures have dramatically outpaced that of

innovative, inexpensive, and easy-to-use true 3D data visualization methods. As a result, progressively more detailed and larger datasets" have been visualized using inherently two-dimensional devices (e.g., computer screens and interactive displays). Despite the introduction of "3D-ready" displays and the progressive increase in terms of pixel resolution, these devices do not allow a true three-dimensional visualization of the collected datasets. In this sense, the recent development and introduction of MR and VR systems represents a significant upgrade in the field of geotechnical and geological data visualization. The progressive miniaturization of electronic components and the dramatic increase in computational capabilities of computer systems will in the near future significantly enhance the applicability of MR and VR technologies to geotechnical data analysis. In this paper, we demonstrated the potential for advanced visualization techniques to enhance interpretation of geological data. However, we emphasize that a reliable interpretation of field and RS datasets through VR and MR methods cannot be possible without an adequate understanding of the geological and geomorphological processes that can affect the investigated site as well as their implications for its evolution.

References

1. Einstein, H.H.; Veneziano, D.; Baecher, G.B.; O'Reilly, K.J. The Effect of Discontinuity Persistence on Rock Slope Stability. *Int. J. Rock Mech. Min. Sci. Geomech. Abstr.* **1983**, *20*, 227–236. [CrossRef]
2. Hoek, E.; Brown, E.T. The Hoek–Brown Failure Criterion and GSI—2018 Edition. *J. Rock Mech. Geotech. Eng.* **2019**, *11*, 445–463. [CrossRef]
3. ISRM Suggested Methods for the Quantitative Description of Discontinuities in Rock Masses. *Int. J. Rock Mech. Min. Sci. Geomech. Abstr.* **1978**, *15*, 319–368. [CrossRef]
4. Barton, N. The Shear Strength of Rock and Rock Joints. *Int. J. Rock Mech. Min. Sci. Geomech. Abstr.* **1976**, *13*, 255–279. [CrossRef]
5. Stead, D.; Donati, D.; Wolter, A.; Sturzenegger, M. Application of Remote Sensing to the Investigation of Rock Slopes: Experience Gained and Lessons Learned. *ISPRS Int. J. Geo-Inf.* **2019**, *8*, 296. [CrossRef]
6. Sturzenegger, M.; Stead, D. Close-Range Terrestrial Digital Photogrammetry and Terrestrial Laser Scanning for Discontinuity Characterization on Rock Cuts. *Eng. Geol.* **2009**, *106*, 163–182. [CrossRef]
7. Donati, D.; Stead, D.; Brideau, M.A.; Ghirotti, M. Using Pre-Failure and Post-Failure Remote Sensing Data to Constrain the Three-Dimensional Numerical Model of a Large Rock Slope Failure. *Landslides* **2021**, *18*, 827–847. [CrossRef]
8. Jaboyedoff, M.; Oppikofer, T.; Abellán, A.; Derron, M.-H.; Loye, A.; Metzger, R.; Pedrazzini, A. Use of LIDAR in Landslide Investigations: A Review. *Nat. Hazards* **2012**, *61*, 5–28. [CrossRef]
9. Guerin, A.; Jaboyedoff, M.; Collins, B.D.; Derron, M.H.; Stock, G.M.; Matasci, B.; Boesiger, M.; Lefeuvre, C.; Podladchikov, Y.Y. Detection of Rock Bridges by Infrared Thermal Imaging and Modeling. *Sci. Rep.* **2019**, *9*, 13138. [CrossRef]
10. Abellán, A.; Jaboyedoff, M.; Oppikofer, T.; Vilaplana, J.M. Detection of Millimetric Deformation Using a Terrestrial Laser Scanner: Experiment and Application to a Rockfall Event. *Nat. Hazards Earth Syst. Sci.* **2009**, *9*, 365–372. [CrossRef]

11.   Atzeni, C.; Barla, M.; Pieraccini, M.; Antolini, F. Early Warning Monitoring of Natural and Engineered Slopes with Ground-Based Synthetic-Aperture Radar. *Rock Mech. Rock Eng.* **2015**, *48*, 235–246. [CrossRef]

12.   Corsini, A.; Castagnetti, C.; Bertacchini, E.; Rivola, R.; Ronchetti, F.; Capra, A. Integrating Airborne and Multi-Temporal Long-Range Terrestrial Laser Scanning with Total Station Measurements for Mapping and Monitoring a Compound Slow Moving Rock Slide. *Earth Surf. Process. Landf.* **2013**, *38*, 1330–1338. [CrossRef]

13.   Stumpf, A.; Malet, J.P.; Allemand, P.; Pierrot-Deseilligny, M.; Skupinski, G. Ground-Based Multi-View Photogrammetry for the Monitoring of Landslide Deformation and Erosion. *Geomorphology* **2015**, *231*, 130–145. [CrossRef]

14.   Kenner, R.; Gischig, V.; Gojcic, Z.; Quéau, Y.; Kienholz, C.; Figi, D.; Thöny, R.; Bonanomi, Y. The Potential of Point Clouds for the Analysis of Rock Kinematics in Large Slope Instabilities: Examples from the Swiss Alps: Brinzauls, Pizzo Cengalo and Spitze Stei. *Landslides* **2022**, *19*, 1357–1377. [CrossRef]

15.   Kromer, R.A.; Abellán, A.; Hutchinson, D.J.; Lato, M.; Chanut, M.-A.; Dubois, L.; Jaboyedoff, M. Automated Terrestrial Laser Scanning with Near-Real-Time Change Detection—Monitoring of the Séchilienne Landslide. *Earth Surf. Dyn.* **2017**, *5*, 293–310. [CrossRef]

16.   Williams, J.G.; Rosser, N.J.; Hardy, R.J.; Brain, M.J.; Afana, A.A. Optimising 4-D Surface Change Detection: An Approach for Capturing Rockfall Magnitude–Frequency. *Earth Surf. Dyn.* **2018**, *6*, 101–119. [CrossRef]

17.   Shan, J.; Toth, C.K. *Topographic Laser Ranging and Scanning. Principles and Processing*; Taylor & Francis Group: Boca Raton, FL, USA, 2008; ISBN 978-1-4200-5142-1.

18.   Westoby, M.J.; Brasington, J.; Glasser, N.F.; Hambrey, M.J.; Reynolds, J.M. "Structure-from-Motion" Photogrammetry: A Low-Cost, Effective Tool for Geoscience Applications. *Geomorphology* **2012**, *179*, 300–314. [CrossRef]

19.   Giordan, D.; Godone, D.; Baldo, M.; Piras, M.; Grasso, N.; Zerbetto, R. Survey Solutions for 3D Acquisition and Representation of Artificial and Natural Caves. *Appl. Sci.* **2021**, *11*, 6482. [CrossRef]

20.   Menegoni, N.; Giordan, D.; Perotti, C.; Tannant, D.D. Detection and Geometric Characterization of Rock Mass Discontinuities Using a 3D High-Resolution Digital Outcrop Model Generated from RPAS Imagery—Ormea Rock Slope, Italy. *Eng. Geol.* **2019**, *252*, 145–163. [CrossRef]

21.   Francioni, M.; Stead, D.; Clague, J.J.; Westin, A. Identification and Analysis of Large Paleo-Landslides at Mount Burnaby, British Columbia. *Environ. Eng. Geosci.* **2018**, *24*, 221–235. [CrossRef]

22.   Clark, M.R.; McCann, D.M.; Forde, M.C. Application of Infrared Thermography to the Non-Destructive Testing of Concrete and Masonry Bridges. *NDT E Int.* **2003**, *36*, 265–275. [CrossRef]

23.   Röper, T.; Greskowiak, J.; Massmann, G. Detecting Small Groundwater Discharge Springs Using Handheld Thermal Infrared Imagery. *Groundwater* **2014**, *52*, 936–942. [CrossRef]

24.   Baroň, I.; Bečkovský, D.; Míča, L. Application of Infrared Thermography for Mapping Open Fractures in Deep-Seated Rockslides and Unstable Cliffs. *Landslides* **2014**, *11*, 15–27. [CrossRef]

25.   Teza, G.; Marcato, G.; Pasuto, A.; Galgaro, A. Integration of Laser Scanning and Thermal Imaging in Monitoring Optimization and Assessment of Rockfall Hazard: A Case History in the Carnic Alps (Northeastern Italy). *Nat. Hazards* **2015**, *76*, 1535–1549. [CrossRef]

26.   Pappalardo, G.; Mineo, S.; Zampelli, S.P.; Cubito, A.; Calcaterra, D. InfraRed Thermography Proposed for the Estimation of the Cooling Rate Index in the Remote Survey of Rock Masses. *Int. J. Rock Mech. Min. Sci.* **2016**, *83*, 182–196. [CrossRef]

27.   Mineo, S.; Pappalardo, G.; Rapisarda, F.; Cubito, A.; Maria, G.D. Integrated Geostructural, Seismic and Infrared Thermography Surveys for the Study of an Unstable Rock Slope in the Peloritani Chain (NE Sicily). *Eng. Geol.* **2015**, *195*, 225–235. [CrossRef]

28.   Frodella, W.; Morelli, S.; Gigli, G.; Casagli, N. Contribution of Infrared Thermography to the Slope Instability Characterization. In Proceedings of the World Landslide Forum 3, Beijing, China, 2–6 June 2014; pp. 97–103.

29.   van der Meer, F.D.; van der Werff, H.M.A.; van Ruitenbeek, F.J.A.; Hecker, C.A.; Bakker, W.H.; Noomen, M.F.; van der Meijde, M.; Carranza, E.J.M.; de Smeth, J.B.; Woldai, T. Multi- and Hyperspectral Geologic Remote Sensing: A Review. *Int. J. Appl. Earth Obs. Geoinf.* **2012**, *14*, 112–128. [CrossRef]

30.   Riaza, A.; Strobl, P.; Beisl, U.; Hausold, A.; Müller, A. Spectral Mapping of Rock Weathering Degrees on Granite Using Hyperspectral DAIS 7915 Spectrometer Data. *ITC J.* **2001**, *3*, 345–354. [CrossRef]

31.   Debba, P.; Carranza, E.J.M.; Stein, A.; van der Meer, F.D. Deriving Optimal Exploration Target Zones on Mineral Prospectivity Maps. *Math. Geosci.* **2009**, *41*, 421–446. [CrossRef]

32.   Kurz, T.H.; Buckley, S.J.; Howell, J. A Close-Range Hyperspectral Imaging for Geological Field Studies: Workflow and Methods. *Int. J. Remote Sens.* **2013**, *34*, 1798–1822. [CrossRef]

33.   Murphy, R.J.; Schneider, S.; Monteiro, S.T. Mapping Layers of Clay in a Vertical Geological Surface Using Hyperspectral Imagery: Variability in Parameters of SWIR Absorption Features under Different Conditions of Illumination. *Remote Sens.* **2014**, *6*, 9104–9129. [CrossRef]

34.   Calvin, W.M.; Pace, E.L. Mapping Alteration in Geothermal Drill Core Using a Field Portable Spectroradiometer. *Geothermics* **2016**, *61*, 12–23. [CrossRef]

35.   Milgram, P.; Kishino, F. A Taxonomy of Mixed Reality Visual Displays. *IEICE Trans. Inf. Syst.* **1994**, *E77*, 1321–1329.

36.   WayRay. Available online: https://wayray.com/ (accessed on 15 March 2023).

37.   Brepohl, P.C.A.; Leite, H. Virtual Reality Applied to Physiotherapy: A Review of Current Knowledge. *Virtual Real.* **2023**, *27*, 71–95. [CrossRef]

38. Choi, S.; Jung, K.; Noh, S.D. Virtual Reality Applications in Manufacturing Industries: Past Research, Present Findings, and Future Directions. *Concurr. Eng.* **2015**, *23*, 40–63. [CrossRef]

39. Product—Clirio, Inc. Available online: https://clir.io/product/ (accessed on 15 March 2023).

40. Onsel, E.; Chang, O.; Mysiorek, J.; Donati, D.; Stead, D.; Barnett, W.; Zorzi, L. Applications of Mixed and Virtual Reality Techniques in Site Characterization Multi-Sensor Remote Sensing Techniques Site Characterization with MR/VR. In Proceedings of the 26th Vancouver Geotechnical Society Symposium, Vancouver, BC, Canada, 31 May 2019.

41. Chang, O. Application of Mixed and Virtual Reality in Geoscience and Engineering Geology. Master's Thesis, Simon Fraser University, Burnaby, BC, Canada, 2019. Available online: https://summit.sfu.ca/item/34761 (accessed on 15 March 2023).

42. Riegl RiSCAN PRO 2.6. 2018. Available online: http://www.riegl.com/products/software-packages/riscan-pro/ (accessed on 15 March 2023).

43. Agisoft Agisoft Metashape 1.5. 2020. Available online: https://www.agisoft.com/ (accessed on 15 March 2023).

44. FLIR ResearchIR 4.4. 2019. Available online: https://www.flir.com/support-center/Instruments/researchir/ (accessed on 15 March 2023).

45. L3 Harris Geospatiale ENVI®Geospatial Image Analysis Software 5.5. 2019. Available online: https://www.l3harrisgeospatial.com/Software-Technology/ENVI (accessed on 15 March 2023).

46. Lichtenauer, J.F.; Sirmacek, B. A Semi-Automatic Procedure for Texturing of Laser Scanning Point Clouds with Google Streetview Images. *Int. Arch. Photogramm. Remote Sens. Spat. Inf. Sci. ISPRS Arch.* **2015**, *40*, 109–114. [CrossRef]

47. Eaton, J.; Bateman, D.; Hauberg, S.; Webhring, R. GNU Octave Version 8.1.0 Manual: A High-Level Interactive Language for Numerical Computations. 2023. Available online: https://octave.org/ (accessed on 20 May 2023).

48. Meshlab 2022.02. 2022. Available online: https://www.meshlab.net/ (accessed on 15 March 2023).

49. CloudCompare. CloudCompare 2.12 [GPL Software]. 2022. Available online: https://www.danielgm.net/cc/ (accessed on 15 March 2023).

50. Donati, D.; Stead, D.; Lato, M.; Gaib, S. Spatio-Temporal Characterization of Slope Damage: Insights from the Ten Mile Slide, British Columbia, Canada. *Landslides* **2020**, *17*, 1037–1049. [CrossRef]

51. Mysiorek, J.; Onsel, E.; Stead, D.; Rosser, N.J. Engineering Geological Characterization of the 2014 Jure Landslide, Nepal: An Interactive Mixed-Reality Approach to Slope Characterization. In Proceedings of the Under Land and Sea. GeoStJohn 2019—72nd Canadian Geotechnical Conference, St. John's, NL, Canada, 29 September–2 October 2019.

52. Unity Unity—Game Engine 2020. Available online: https://www.unity.com/ (accessed on 15 March 2023).

53. Blender Development Team Blender 2.93 LTS. 2022. Available online: https://www.blender.org/ (accessed on 15 March 2023).

54. Cairnes, C.E. *Coquihalla Area, British Columbia*; FA Acland: Ottawa, ON, Canada, 1924; 193p.

55. Berman, R.G.; Armstrong, R.L. Geology of the Coquihalla Volcanic Complex, Southwestern British Columbia. *Can. J. Earth Sci.* **1980**, *17*, 985–995. [CrossRef]

56. Tuckey, Z. An Integrated Field Mapping-Numerical Modelling Approach to Characterising Discontinuity Persistence and Intact Rock Bridges in Large Open Pit Slopes. M.Sc. Thesis, Simon Fraser University, 2012. Available online: https://summit.sfu.ca/item/12708 (accessed on 10 April 2023).

57. Leith, K.; Moore, J.R.; Amann, F.; Loew, S. In Situ Stress Control on Microcrack Generation and Macroscopic Extensional Fracture in Exhuming Bedrock. *J. Geophys. Res.* **2014**, *119*, 594–615. [CrossRef]

58. Paronuzzi, P.; Bolla, A. In-Depth Field Survey of a Rockslide Detachment Surface to Recognise the Occurrence of Gravity-Induced Cracking. *Eng. Geol.* **2022**, *302*, 106636. [CrossRef]

59. de Vilder, S.J.; Rosser, N.J.; Brain, M.J. Forensic Analysis of Rockfall Scars. *Geomorphology* **2017**, *295*, 202–214. [CrossRef]

60. McMechan, M.A. *Rocky Mountain Foothills and Front Ranges in Kananaskis Country, West of Fifth Meridian, Alberta, Geological Survey of Canada, "A" Series Map 1865A, 1995, 1 Sheet*; Natural Resources Canada: Ottawa, ON, Canada, 1995. [CrossRef]

61. Zechmeister, M.S.; Pannalal, S.; Elmore, R.D. A Multidisciplinary Investigation of Multiple Remagnetizations within the Southern Canadian Cordillera, SW Alberta and SE British Columbia. *Geol. Soc. Lond. Spec. Publ.* **2012**, *371*, 123–144. [CrossRef]

62. Price, R.A. The Cordilleran Foreland Thrust and Fold Belt in the Southern Canadian Rocky Mountains. *Geol. Soc. Lond. Spec. Publ.* **1981**, *9*, 427–448. [CrossRef]

63. Upreti, B.N. An Overview of the Stratigraphy and Tectonics of the Nepal Himalaya. *J. Asian Earth Sci.* **1999**, *17*, 577–606. [CrossRef]

64. Dhital, M.R. *Geology of the Nepal Himalaya*; Regional Geology Reviews; Springer International Publishing: Cham, Switzerland, 2015; ISBN 978-3-319-02495-0.

65. Champati ray, P.K.; Chattoraj, S.L. Sunkoshi Landslide in Nepal and Its Possible Impact in India: A Remote Sensing Based Appraisal. In Proceedings of the International Archives of the Photogrammetry, Remote Sensing and Spatial Information Sciences, Hyderabad, India, 9–12 December 2014; Copernicus GmbH: Göttingen, Germany, 2014; Volume XL–8, pp. 1345–1351.

66. Shrestha, B.B.; Nakagawa, H. Hazard Assessment of the Formation and Failure of the Sunkoshi Landslide Dam in Nepal. *Nat. Hazards* **2016**, *82*, 2029–2049. [CrossRef]

67. Mysiorek, J. Engineering Geological Characterization of the 2014 Jure Nepal Landslide: An Integrated Field, Remote Sensing-Virtual/Mixed Reality Approach. Master's Thesis, Simon Fraser University, Burnaby, BC, Canada, 2019. Available online: https://summit.sfu.ca/item/19917 (accessed on 10 March 2023).

68. Thiele, S.T.; Grose, L.; Samsu, A.; Micklethwaite, S.; Vollgger, S.A.; Cruden, A.R. Rapid, Semi-Automatic Fracture and Contact Mapping for Point Clouds, Images and Geophysical Data. *Solid Earth* **2017**, *8*, 1241–1253. [CrossRef]
69. Rocscience RocFall2. 2022. Available online: https://www.rocscience.com/software/rocfall (accessed on 15 March 2023).
70. ESRI ArcMap 10.6. 2019. Available online: https://www.esri.com/ (accessed on 15 March 2023).
71. Orpen, J.L. Best Practice and New Technology in Core Drilling, Logging and Fracture Analysis. In Proceedings of the 1st International Conference on Discrete Fracture Network Engineering, Vancouver, BC, Canada, 19 October 2014.
72. SRK Consulting EasyMineXR Collaborative Mapping Software. 2022. Available online: https://www.srk.com/en/products/easyminexr-collaborative-mapping-software (accessed on 15 April 2023).
73. Onsel, I.E.; Donati, D.; Stead, D.; Chang, O. Applications of Virtual and Mixed Reality in Rock Engineering. In Proceedings of the 52nd U.S. Rock Mechanics/Geomechanics Symposium, Washington, DC, USA, 17–20 June 2018.
74. Seequent Leapfrog Geo. 2022. Available online: https://www.seequent.com/products-solutions/leapfrog-geo/ (accessed on 15 April 2023).
75. Hammah, R.E.; Curran, J.H. On Distance Measures for the Fuzzy K-Means Algorithm for Joint Data. *Rock Mech. Rock Eng.* **1999**, *32*, 1–27. [CrossRef]
76. Barton, N.; Choubey, V. The Shear Strength of Rock Joints in Theory and Practice. *Rock Mech. Felsmech. Mec. Roches* **1977**, *10*, 1–54. [CrossRef]
77. Deere, D.U.; Deere, D.W. *Rock Quality Designation (RQD) after Twenty Years*; Defense Techniccal Information Centre: Fort Belvoir, VA, USA, 1989; ADA207597. Available online: https://apps.dtic.mil/sti/citations/ADA207597 (accessed on 15 April 2023).
78. NGI. *Using the Q-System. Rock Mass Classification and Support Design*; NGI: Oslo, Norway, 2022.
79. Pells, P.J.; Bieniawski, Z.T.; Hencher, S.R.; Pells, S.E. Rock Quality Designation (RQD): Time to Rest in Peace. *Can. Geotech. J.* **2017**, *54*, 825–834. [CrossRef]